Laser-induced carbonization of stainless steel as a corrosion mitigation strategy for high-temperature molten salts applications

González-Fernández, Luis; Anagnostopoulos, Argyrios; Karkantonis, Themistoklis; Bondarchuk, Oleksandr; Dimov, Stefan; Chorążewski, Mirosław; Ding, Yulong; Grosu, Yaroslav

DOI:
10.1016/j.est.2022.105972

Document Version
Publisher's PDF, also known as Version of record

Citation for published version (Harvard):
González-Fernández, L, Anagnostopoulos, A, Karkantonis, T, Bondarchuk, O, Dimov, S, Chorążewski, M, Ding, Y & Grosu, Y 2022, 'Laser-induced carbonization of stainless steel as a corrosion mitigation strategy for high-temperature molten salts applications', *Journal of Energy Storage*, vol. 56, 105972. https://doi.org/10.1016/j.est.2022.105972

Journal of Energy Storage 56 (2022) 105972

Contents lists available at ScienceDirect

Journal of Energy Storage

journal homepage: www.elsevier.com/locate/est

Research Papers

Laser-induced carbonization of stainless steel as a corrosion mitigation strategy for high-temperature molten salts applications

Luis González-Fernández [a], Argyrios Anagnostopoulos [b,c,*], Themistoklis Karkantonis [d], Oleksandr Bondarchuk [e], Stefan Dimov [d], Mirosław Chorążewski [c], Yulong Ding [b], Yaroslav Grosu [a,c,*]

[a] Centre for Cooperative Research on Alternative Energies (CIC energiGUNE), Basque Research and Technology Alliance (BRTA), Alava Technology Park, Albert Einstein 48, 01510 Vitoria-Gasteiz, Spain
[b] BCES Birmingham Centre of Energy Storage, University of Birmingham, United Kingdom
[c] Institute of Chemistry, University of Silesia, 40-006 Katowice, Poland
[d] Department of Mechanical Engineering, School of Engineering, The University of Birmingham, Birmingham, B15 2TT, UK
[e] International Iberian Nanotechnology Laboratory, Av. Mestre José Veiga, s/n, 4715-330 Braga, Portugal

ARTICLE INFO

Keywords:
Molten salt
Corrosion
Stainless steel
Mitigation
Nanosecond laser

ABSTRACT

New heat transfer fluids are necessary to shift the operation temperature of concentrating solar power plants (CSP) to higher temperatures. Ternary carbonate salts (Li_2CO_3-K_2CO_3-Na_2CO_3) are a promising candidate. However, higher temperature translates to harsher operating conditions for CSP structural components as corrosion is more prevalent. In this work, we explore, for the first time, the use of laser micro-machining technology as a surface modification method to inhibit corrosion of CSP structural materials by molten salts. The corrosion behaviour of SS310 in molten ternary carbonate salt is investigated through static immersion for 600 h. Nanosecond laser treatment results in the adhesion of organic groups in the form of hydrocarbons. These then decompose into carbon and contribute to corrosion inhibition through carbonization and the formation of carbide layers. This is confirmed by the reduced diffusion of Li + ions in the SS310, the formation of denser corrosion products and the protection of chromium oxide layers.

1. Introduction

Currently, fossil fuel-based energy is used to power roughly 80 % of the total global energy demand [1]. Dependency on non-sustainable pathways to generate energy coupled with a rapidly growing global energy demand has led to considerable environmental challenges [1]. A sustainable solution to these issues is the high penetration of renewable energy, with the sun being the most abundant source of "clean energy" [2].

Concentrating solar power (CSP) is a technology complementary to photovoltaics. It uses concentrating collectors to accumulate high-temperature heat and feed it into a conventional power cycle where it is transformed into electric energy. CSP has been around since the 1960s, but massive adoption started in 2007, primarily in the United States and Spain [3]. More recently, installations have been implemented in the Middle East, North and South Africa, as well as India and China, bringing the total install capacity in 2020 at 14.5 TWh, with a projected 204 TWh by 2030 [4].

CSP, although a mature technology, still has room for improvement. Increasing the operating temperature has been shown to considerably improve the power cycle efficiency, thus increasing capacity and decreasing levelized costs [5]. Currently, most CSP plants utilize a mixture of molten nitrate salts, the so-called solar salt (SS), both as a heat transfer fluid to transport the heat concentrated at the receiver as well as a thermal energy storage medium [6,7]. SS, however, has a maximum operating temperature of 565 °C [8]. NextGen CSP plants are, therefore, looking for alternative mediums for heat transfer and storage. Molten salts are well established in CSP due to their good heat capacity, high density and low vapour pressure. Of these salts, the best options for the next Gen plants are molten chloride and carbonate salts.

Chloride salts, although more economically competitive, suffer from poor compatibility with structural materials used in CSP plants [9,10]. Extensive corrosion studies of steels and alloys in molten chloride and carbonate salts have reported substantially higher corrosion rates in

* Corresponding authors at: Institute of Chemistry, University of Silesia, 40-006 +Katowice, Poland.
E-mail addresses: a.anagnostopoulos@bham.ac.uk (A. Anagnostopoulos), ygrosu@cicenergigune.com (Y. Grosu).

https://doi.org/10.1016/j.est.2022.105972
Received 1 August 2022; Received in revised form 5 October 2022; Accepted 24 October 2022
Available online 7 November 2022

chlorides [11]. Therefore, despite being more expensive, carbonate salts are still explored. Among various carbonate salts, the eutectic LiNaK carbonate salt (32.1 wt% Li_2CO_3; 33.4 wt% Na_2CO_3; 34.5 wt% K_2CO_3) is widely recognized as the most competitive alternative [12].

Coyel et al. were the first researchers to investigate the corrosion of LiNaK salts in CSP structural materials. They evaluated the corrosion performance of a series of alloys in contact with LiNaK at 900 °C and found Inconel 600 to be the most compatible [13]. More recently, Takeuchi et al. investigated the performance of Fe—Cr alloys in molten Li_2CO_3/K_2CO_3 and found that the thickness of the outer and mid-layer decreases with increasing Cr content [14]. This was further verified by Ahn et al., who observed a higher corrosion resistance of 310S compared to 316 L, which was attributed to the lower Cr content of the latter [15]. Miguel et al. studied the corrosion behaviour of molten ternary in contact with HR3C at 700 °C for up to 2000 h. He noted that an initial layer of chromium was formed on the metallic surface that was later dissolved in the salt leaving a multilayer structure primarily consisting of iron oxide, nickel and chromium [16]. Similar results were reported by the same group in a study of HR3C immersed in molten carbonate ternary. They further reported that corrosion was accelerated at 800 °C compared to 700 °C [17]. This was also confirmed by Luo et al. in a compatibility study of SS316 with LiNaK at 600 °C and 700 °C [18]. Sah et al. conducted an electrochemical study of molten carbonate ternary in contact with 310S, 316 L, and 304 in a CO_2:O_2 = 2:1 atm and reported 310S having the highest and 304 the poorest corrosion resistance. This was linked to Cr and Ni contents, with Cr-content linked to the highest passivation [19]. In a study by Gonzalez et al., the corrosion rate on AISI316 by molten ternary carbonate salt was found to be 2.07 mm/yr at 600 °C. The authors noted that the content of Li_2CO_3 slows the corrosion rate [20]. Sarvghad et al. reported a positive effect of annealing on the corrosion of Inconel 601 as well as SS316L by LiNaK at 450 °C. Annealing was linked to more uniform grain boundaries and density of dislocations that mitigates intergranular failure, which is the main reason for stress-assisted oxidation [21–23].

In view of the above, molten LiNaK is a promising candidate for next-gen CSP plants. However, its compatibility with structural material candidates is poor in the projected operational time frame of CSP plants (25 years). Efforts are ongoing to develop novel methods to mitigate corrosion. This is either through doping the molten salt with additives or through modification of the metallic surface properties [24–26]. Fragnini and Loreti reported decreased corrosion rates of SS316L in molten LiNaK at 650 °C with the addition of Mg and Ca ions at concentrations <10 % mol [27]. We recently proposed a simple spray-graphitization method for corrosion mitigation of SS310 and SS347 by molten LiNaK at 650 °C. Graphite spraying led to the formation of an iron carbide/carbonate layer that reduced Cr diffusion, thus inhibiting further oxidation [28,29].

Surface modification methods have recently emerged as promising candidates for molten salt corrosion mitigation. Kondaiah and Pitchumani induced a multiscale fractal texturing on SS316, In800H, In718, In625, and Ha230 via chemical etching and annealing. They demonstrated corrosion mitigation in 60 % $NaNO_3$ + 40 % KNO_3 at 600 °C of up to 87 % when compared to plain surfaces. It was found that the of the initially grown oxides of spinels on the etched surfaces act as passive layers and prevent further deterioration [30]. In addition, laser micromachining technology has widely been used as a method to tailor the functional response of materials by modifying their surface topography and/or chemistry. Thus, it has been effectively employed to improve the corrosion resistance of stainless steel, alloys and aluminium surfaces in aqueous solutions [31–33]. Quite recently, Fan et al. used an ultrashort pulsed laser for polishing yttria-stabilized zirconia coatings to mitigate corrosion by Na_2SO_4 + V_2O_5 at 1000 °C. The polishing resulted in a smooth, uniform surface with healed voids that alleviated diffusion [34].

This work serves as a proof-of-concept study of nanosecond laser-induced carbonization as an approach for corrosion mitigation of metallic surfaces in molten salts. Irradiation of stainless steel samples with nanosecond laser pulses has been shown to promote silanization [35]. Here we observe the formation of silanes at the surface of an SS310 after laser treatment that are then transformed into iron carbides and carbonates during the corrosion test. These layers mitigate corrosion evolution. These results are of relevance for a broad range of applications, where high-temperature molten salt corrosion is a major issue, namely, CSP, storage plants, power-to-heat-to-power, fuel cells, nuclear, etc.

1.1. Materials and preparation

Eutectic ternary carbonate salt was employed for the corrosion test: 34.5 % K_2CO_3–33.4 % Na_2CO_3–32.1 % Li_2CO_3 (weight concentration). The components of the ternary salt were purchased from Sigma-Aldrich, with purities higher than 99 %. Before mixing in the correct proportions, the carbonates were dried at 120 °C in the oven for no <12 h. Afterwards, they were weighted and blended.

SS310 samples of 20 × 10 × 2 mm size were used for the corrosion experiments, whose composition is detailed in Table 1. Both surfaces of the pieces were polished up to 1200 SiC sandpaper using ATM Saphir stationary polishing machine. Next, the samples were successively cleaned in acetone, ethanol and distilled water in an ultrasonic bath for 15 min for each solvent.

1.2. Laser surface treatment

The surface texturing experiments were carried out on a laser micromachining system (LASEA LS5, Belgium) under atmospheric conditions. More specifically, the system integrates a nanosecond MOPA-based Yb fibre laser (SPI G4 S-type) with a nominal wavelength of 1064 nm, average power up to 50 W and a maximum repetition rate of 1 MHz. The samples were processed with a circularly polarised Gaussian laser beam ($M^2 < 1.3$), which was focused down to a beam spot diameter of 40 μm at the focal plane using a telecentric lens with a 100 mm focal length. The pulses delivered on their surfaces had a fixed duration of 220 ns. A 3D scan head (Rhothor RTA) was incorporated into the beam delivery sub-system to control the laser beam movements. Thus, it was employed to direct the focused beam across the samples at a scanning speed of 1000 mm/s. Finally, a set of high precession motorised stages was used to position the substrates at the focal plane prior to their laser processing.

A particular laser texturing operation was performed to fabricate highly homogeneous square-shaped micro-pillars onto the surface of the metallic samples by following the strategy and processing window described in another work [36,37]. Briefly, the desired topography was attained by scanning the surface in two perpendicular directions, like a grid, with a constant repetition rate of 65 kHz and pulse fluence of 9 J/cm^2. In the employed grid-like scanning strategy, a constant hatch distance of 100 μm was set between two consecutive lines in both directions to produce micro-grooves on the surface. After repeating the entire procedure five times, bulges from the recast material were formed along the edges of the grooves due to the thermal effects during the nanosecond pulsed laser processing.

After the texturing operation, the patterned surfaces were stored in a laboratory environment for a total of 45 days. This timeframe is considered sufficient for the contact angle to change to superhydrophobic, which confirms that maximum carbon content has accumulated on the surface. Such over-time transition of nanosecond laser processed metallic surfaces in air has been reported by researchers [38].

1.3. Corrosion protocol and experimental setup

The corrosion test was carried out by placing the SS310 samples in alumina crucibles and covering them completely with 25 g of eutectic carbonate salt. The crucibles were inserted into a furnace and heated to

Table 1
Chemical composition (wt%) of tested SS310.

Element	Fe	Ni	Cr	Mn	Si	P	C	S
Concentration	Balance	19.1	24.9	1.81	0.64	0.03	0.05	0.01

600 °C, with a 5 °C/min heating rate. The duration of the experiment was 600 h. Afterwards, the furnace was cooled to 450 °C at 5 °C/min, and the samples were then extracted from the molten salts by tweezers.

1.4. Characterization techniques

1.4.1. Scanning Electron microscopy - SEM

For the SEM analysis, a Quanta 200 FEG model was used in high vacuum mode at 20 kV with a backscattered electron detector (BSED) and an Everhart-Thornley Detector (ETD). Energy-Dispersive X-Ray Spectroscopy (EDX) was performed for elemental mapping. Additionally, FEI Helios NanoLab 450S DualBeam – Focused ion beam (FIB) with FEG SEM was used.

Firstly, the surfaces of all the samples were analysed on both sides. Secondly, the cross-section of samples was checked to further study the corrosion layer. For this purpose, the samples were embedded in a resin holder composed of Aka-Resin and Aka-Cure catalyst (1 mL to 0.135 mL proportion, respectively). When the resin solidifies, it creates a hard shell that protects the corrosion layer from detaching during the cutting and polishing processes. To properly observe the sample's cross-section, the samples underwent progressive polishing with 240, 400, 800, 1200 and 2500 SiC sandpaper using an ATM Saphir stationary polishing machine.

1.4.2. X-ray diffraction - XRD

The X-ray diffraction measurements were carried out using a Bruker D8 Discover X-ray diffractometer equipped with an LYNXEYE detector using CuKα1 radiation (λ = 1.5418 Å) in Bragg-Brentano θ:2θ geometry. The data collection was carried out at room temperature, between 10^{o} and 80^{o}, with a step size of 0.02^{o} and a collection time of 1 s/step. Later, the phase identification of each sample was performed by EVA software.

1.4.3. X-ray photoelectron spectroscopy characterization – XPS

The XPS measurements were performed in an ultra-high vacuum (UHV) system ESCALAB250Xi (Thermo Fisher Scientific). The base pressure in the system was below $5{\cdot}10^{-10}$ mbar. The XPS spectra were acquired with a hemispherical analyzer, and a monochromated X-ray source (Al K_{α} radiation, h1486.6 = υ eV) operated at 15 keV and 200 W power. The XPS spectra were recorded with pass energies 20 eV and 200 eV for high resolution and survey spectra, respectively. The spectrometer was calibrated by setting the Au 4f7/2 level to 84.0 eV measured on a gold foil.

XPS spectra were peak-fitted using the Avantage data processing software. For peak fitting, the Shirley-type background subtraction was used. Quantification was done using elemental sensitivity factors provided by the Avantage library.

The XPS system features a dual-mode Ar ion source MAGCIS (Thermo Fisher Scientific), which can operate in monoatomic and cluster modes. Before XPS characterization, the surfaces of the samples were cleaned using Ar cluster ions of 1000 atoms. For Ar cluster cleaning, an accelerating voltage of 6 keV was used. For depth profiling, the MAGCIS was operated in the monoatomic mode with beam energy 4 keV and beam current 3 μA.

1.4.4. Inductively coupled plasma optical emission spectroscopy – ICP-OES

Samples were analysed using a Horiba Ultima 2 (Jobin Yvon, Longjumeau, France) in conjunction with an AS500 autosampler and Activanalyst software (version 5.4).

The ICP-OES operating conditions were as follows: 1.0 kW of RF power, 13 l/min of a plasma-gas flow rate, 0.2 l/min of a sheath-gas flow rate and 0.25 l/min of a nebulizer-gas flow rate. Solutions were introduced into the plasma torch using a nebulizer and a cyclonic-type spray chamber at a flow rate of 0.87 mL/min.

A multi-elemental standard solution of 100 mg/l containing 25 elements supplied by Scharlab (Barcelona, Spain) was used for calibration. HNO3 69 % from Scharlab (Barcelona, Spain) analytical grade and Ultrapure Water from Fischer Scientific (Waltham, Massachusetts, USA) were used for dilutions.

1.4.5. FTIR (Fourier transform infrared)

A spectrometer Vertex 80v (Bruker) was deployed for the FTIR measurements operated in the reflectance mode with incident and escape angles of 30^{0}, 45^{0}, and 60^{0} with respect to the surface normal. The sample compartment was evacuated down to ~2 mbar during the measurements. The spectra were referenced against vacuum signal. The number of spectra accumulations was 100 scans with a resolution of 4 cm^{-1}.

2. Results

2.1. Before corrosion test

The first examination of the laser-treated sample (LTS) was optical by means of a macro lens. Fig. 1 presents an image of the sample, where a regular pattern on the surface of the SS310 is observed due to laser texturing. This pattern slightly increased the thickness of the sample. As a reference, the initial thickness of the SS310 piece was approx. 1.9 mm.

The as-prepared LTS was analysed by SEM to evaluate the homogeneity of the surface. As can be seen in Fig. 2, a repetitive pattern was observed across the entire surface. The width of the grooves produced by the laser, together with the area enclosed between the micro-pillar structure, are included in the figure.

The surface topography of the LTS was also analysed by a profilometer. In particular, a surface profile of the pristine LTS, taken perpendicularly to the pattern, is shown in Fig. 3. From this plot, it is evident that the groove structures produced on the surface, i.e. the smaller region between the two peaks, had a width of around 37 μm while the area enclosed between the micro-pillars was measured to be roughly 63 μm. The dimensional characteristics of the grooves and pillars determined from the surface profile are in agreement with the ones measured in the SEM images. Finally, it should be noted that the height of the pillars (surface height increase) was found to be approximately 8 μm.

The content of carbon on the surface of the LTS was quantified by SEM-EDX in the two different regions of the pattern. A significant

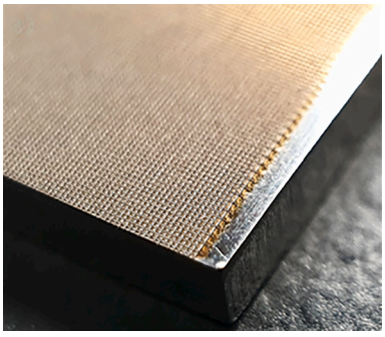

Fig. 1. Optical image of the laser-treated surface of SS310.

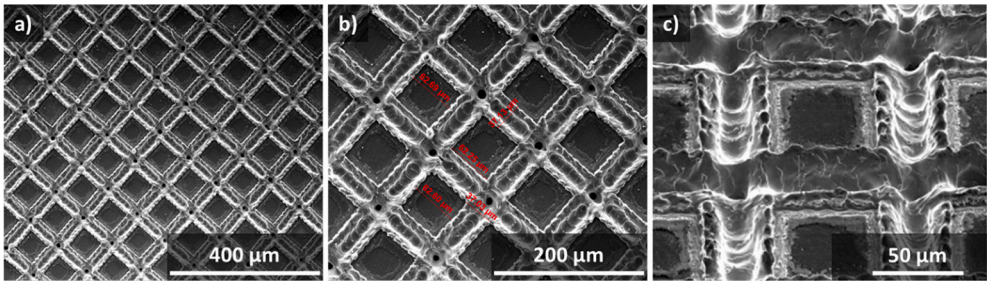

Fig. 2. SEM images of as-prepared LTS.

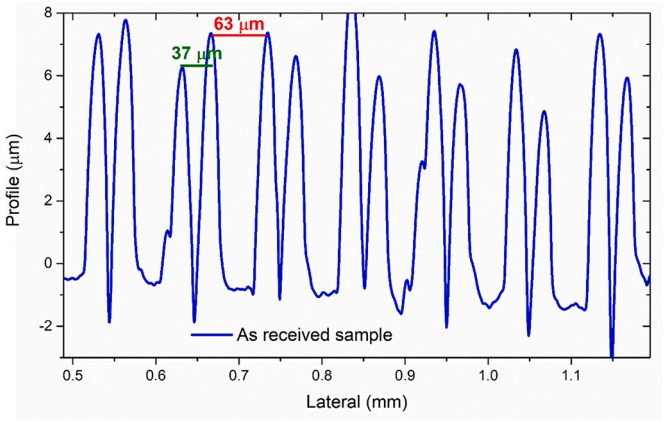

Fig. 3. Roughness profile of the pristine LTS.

amount of C has been detected in the pillars, while no C content is found in the grooves. Additionally, the composition of the pillars considerably differs from one of the grooves and is more similar, apart from the carbon content, to the composition of the untreated SS310 (Fig. 4b). The presence of oxygen in the pillars can be an indication of superficial oxidation of the sample, probably attributable to the energy absorption that takes place during the laser treatment. This is further evidenced by the reduced amount of iron, nickel and chromium content on the square area enclosed by the pillars, as opposed to untreated steel, which indicates the formation of iron and nickel oxides. Similar observations were noted by Rukosuyev et al. on femtosecond processed AISI 316L [39].

The phases present in the LTS's surface have been identified by XRD (Fig. 5). The prominent peaks correspond to the metallic components of the SS310: Fe, Cr and Ni. Additionally, there are minor peaks of magnetite, which agrees with the oxygen present in the previous compositional analysis. However, although carbon was detected in the sample by SEM-EDX, no C-containing phase was present in the diffractogram. This suggests that the carbon incorporated into the SS310 is amorphous.

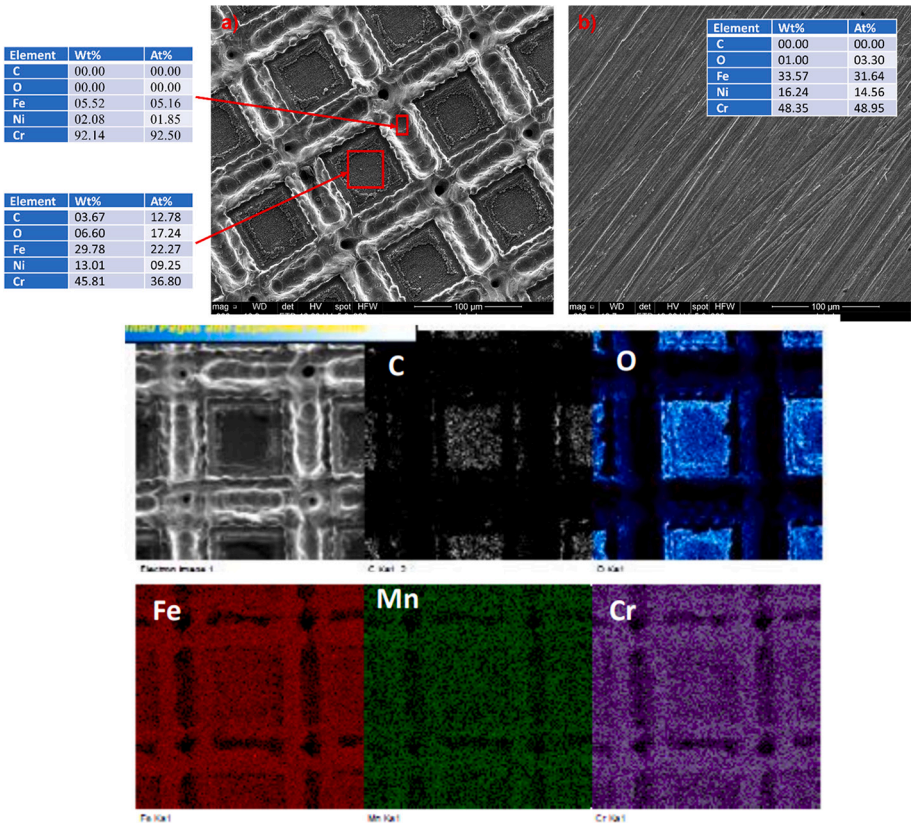

Fig. 4. Compositional analysis obtained by SEM-EDX for (a) laser graphitized and (b) pristine SS310 sample.

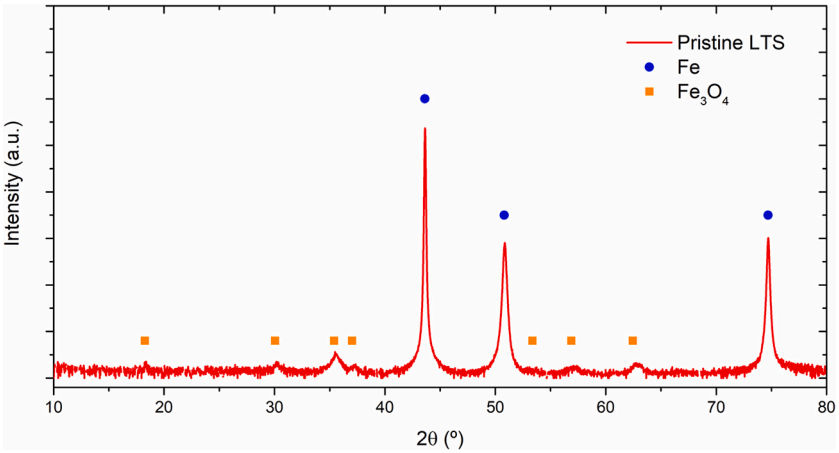

Fig. 5. XRD pattern of the pristine LTS.

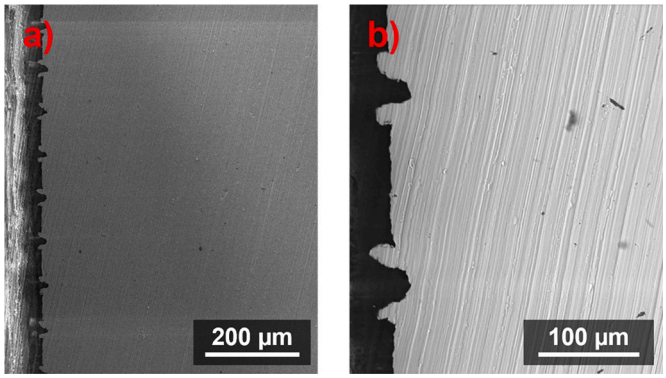

Fig. 6. SEM images of the cross-section of the pristine LTS at different magnifications.

In Fig. 6, the cross-section images of pristine LTS are presented. The sample was cut perpendicularly to one of the directions of the laser pattern and parallel to the other one. The indentations shown in the figure correspond to the groove structures produced after the laser treatment. Although the Fe_3O_4 phase was identified by XRD, no appreciable layer can be observed in the outer region of the LTS.

2.2. *After the corrosion test*

Images of laser-treated and non-treated SS310 samples after the corrosion test are presented in Fig. 7. No peeling of the corrosion layer has occurred during exposure to the molten salt in the case of the LTS. On the contrary, a pronounced detachment is visible in the non-treated SS310 sample. Remarkably, the only appreciable peeling of the LTS is located at the edge of the sample, i.e. the area not textured by laser. This is a visual testament to the corrosion mitigation properties of the LTS. This is further verified by the homogeneity of the LTS, with no pronounced corrosion spots as opposed to the inhomogeneous state of the untreated SS310 sample, which is full of spots and presents a carrying color gradient.

The superficial homogeneity has also been observed by SEM (Fig. 8). After the corrosion test, the pattern produced by the laser is still visible. However, no differences in composition have been detected by SEM-EDX between the grooves and the squares. At the highest magnifications, two different types of crystals are appreciated, a smaller and less regular one and another bigger one with a rhombohedral shape.

For comparison, in Fig. 9, the SEM images of the surface of the non-treated SS310 sample are presented. The non-homogeneity of the corrosion layer can be observed for the lowest magnification image

Fig. 7. Optical images of a) laser-treated and b) non-treated SS310 samples after the corrosion experiment.

(Fig. 9a). Different crystal formations can be seen at higher magnification: tubular formations (Fig. 9b) and irregular crystals (Fig. 9c).

The roughness profile of the LTS after the corrosion test is compared to the initial profile (Fig. 8). It can be observed that the valley located in the middle of the groove has not changed in height or shape. The modification takes place in the squares, whose level has significantly increased due to the corrosion process. This suggests that valleys, where laser ablation took place formed stable oxides, which were not affected during the corrosion test in ternary carbonate salt. On the contrary, the pillars, which were found to be rich with carbon before the corrosion test (Fig. 4), underwent some transformation (Fig. 10).

Fig. 11 shows the XRD curve of the tested LTS, together with the pattern corresponding to graphitized SS310 and non-treated SS310 samples after the same type of corrosion experiment [29]. The diffractograms of laser-treated and graphitized samples are very similar, presenting almost identical phases. This indicates that the laser treatment leads to the formation of a protective layer of carbon-containing with phases similar to those observed in spray-graphitization [29]. Indeed, for the LTS, the presence of the iron carbide and iron carbonate phases is more pronounced than for the spray-graphitization case. This suggests that the carbon-rich pillar regions of patterned SS310 were transformed into protective carbide and carbonate phases.

In Fig. 12, the SEM-EDX analysis of the cross-section for LTS is presented. Combining the results of XRD (Fig. 11) and SEM-EDX mappings, the location of the phases present in the corresponding corrosion layer

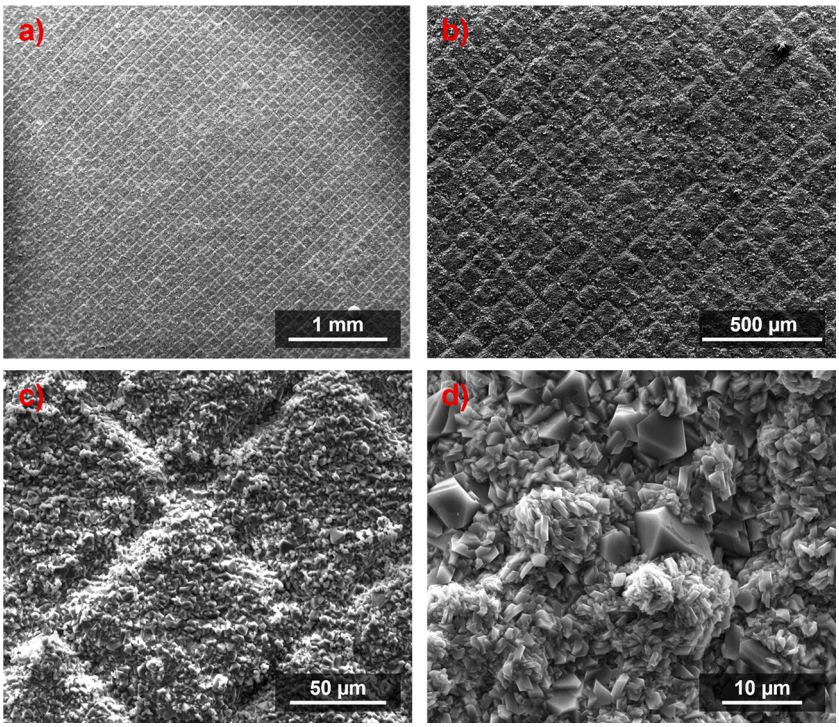

Fig. 8. SEM images of LTS after corrosion test for several magnifications.

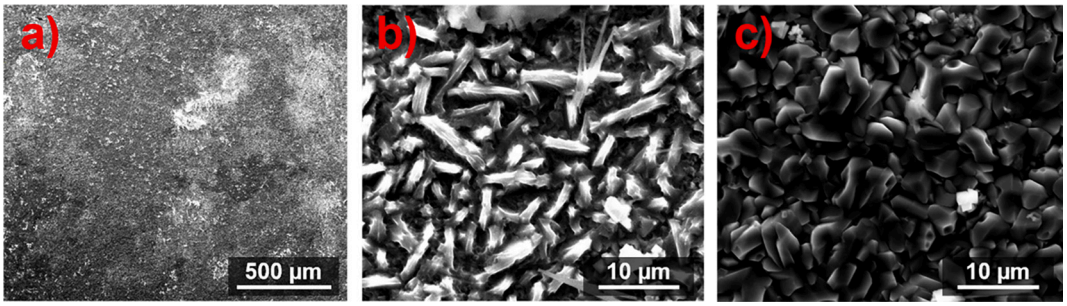

Fig. 9. SEM images of SS310 sample after corrosion test for several magnifications.

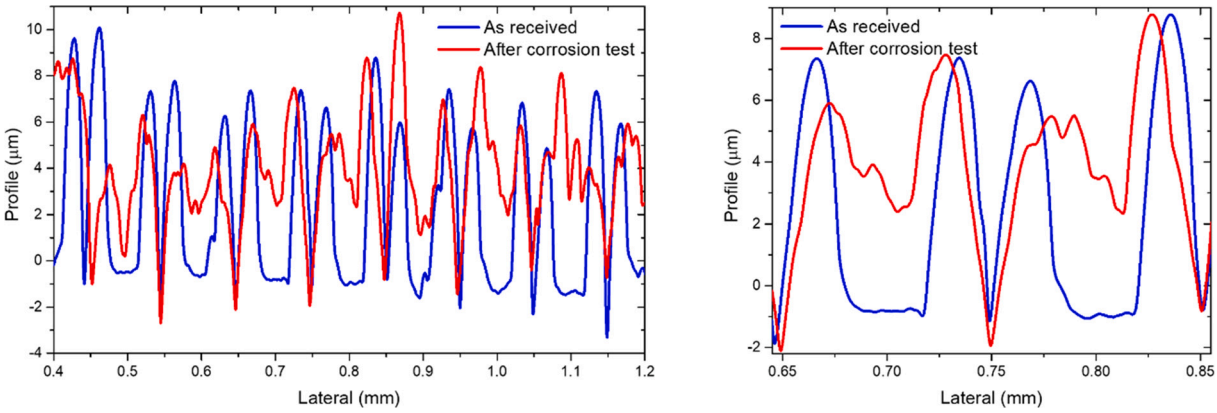

Fig. 10. Roughness profile of the LTS before and after the corrosion test. The figure on the right is a detail for ease the comparison.

can be determined. In the LTS, the mixed Cr oxides containing phases are located in the layer close to the substrate, the darker region, while the Fe mixed oxides grow above that layer. On top of the corrosion scale, carbides and carbonates can be found. The same behaviour is repeated all along the corrosion layer. The corrosion scale is dense and well-attached to the substrate.

In contrast, in reference SS310 (Fig. 13), the respective locations of the layers rich in Cr and Fe are not maintained. In some regions, the

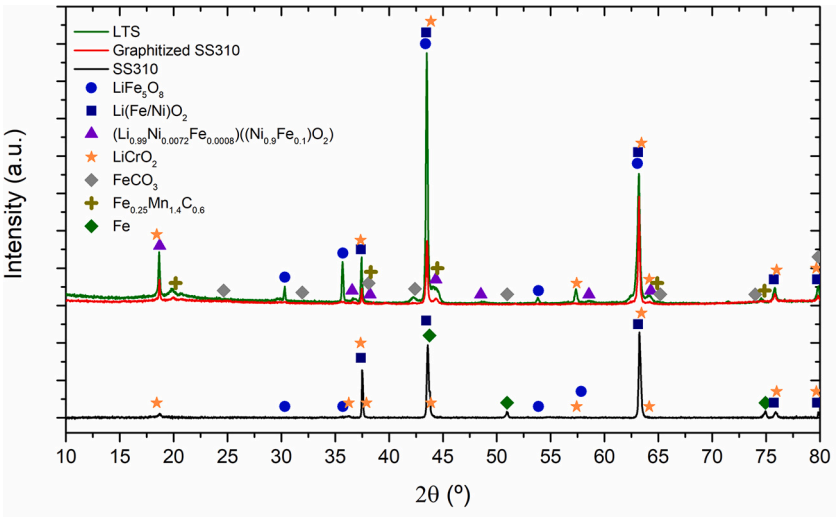

Fig. 11. XRD pattern of LTS and graphitized SS310 [29] after 600 h of corrosion experiment in carbonate salt at 600 °C.

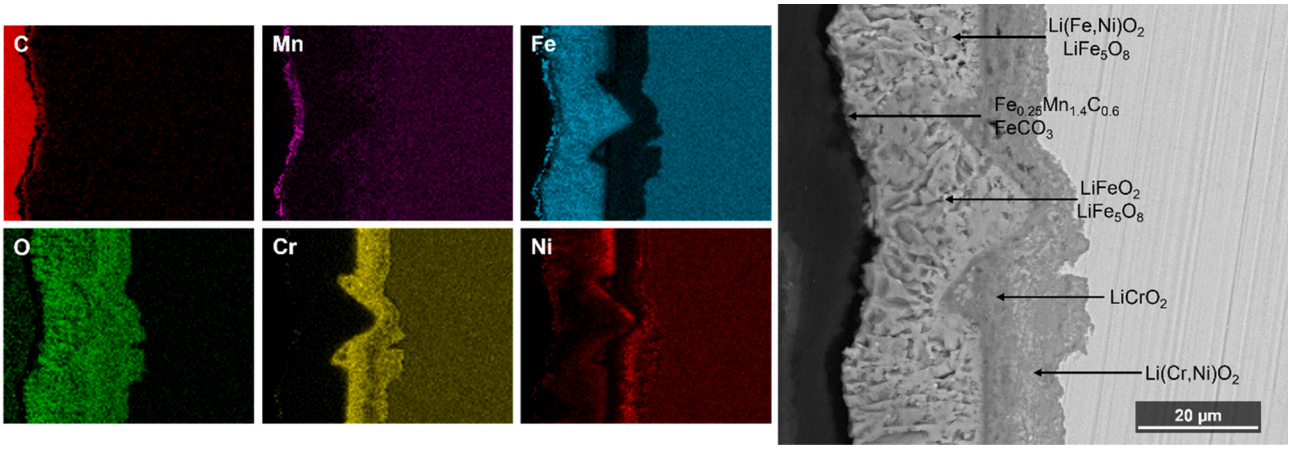

Fig. 12. SEM images and EDX mapping of the cross-section of LTS after 600 h of corrosion experiment at 600 °C.

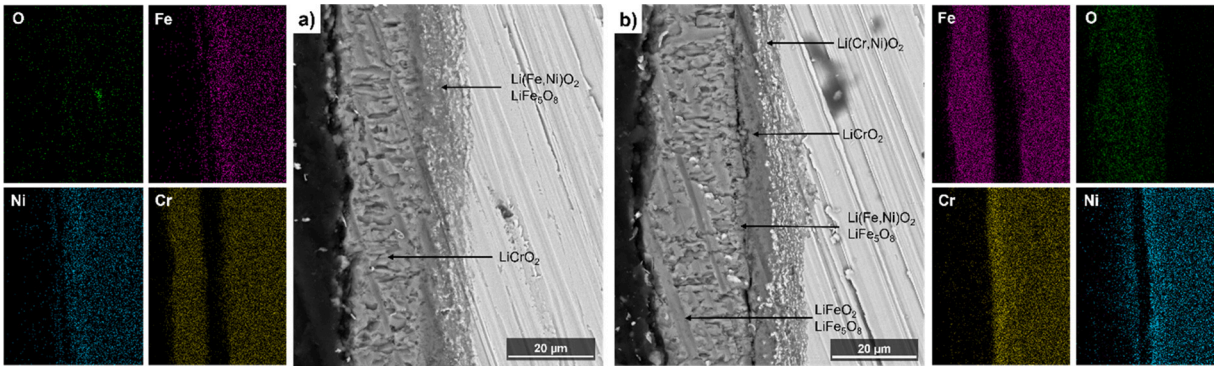

Fig. 13. SEM images and EDX mapping of the cross-section of reference SS310 after 600 h of corrosion experiment at 600 °C.

layer made of $LiCrO_2$ is located on the outer side of the corrosion layer (Fig. 13a), while in other cases, the mixed Cr oxides are placed in the interface between the metallic substrate and the corrosion layer (Fig. 13b). This behaviour is a sign of inhomogeneity, the peeling of the corrosion layer, and the growth of a new layer. Figs. 12 and 13 indicate that the corrosion scale of non-treated SS310 is less regular and dense than LTS.

The average corrosion layer thickness has been determined by analysing the cross-section images by ImageJ software. The thickness has been measured for >250 points to get a representative average value. The corrosion layer thicknesses are 26.9 ± 4.8 µm and 26.6 ± 2.47 µm for LTS and reference SS310 samples, respectively. Thus, in both cases, the corrosion rate is ~390 µm/year. However, considering the peeling-off observed in the regular SS310, which did not happen for the LTS, the corrosion extent can be assumed to be reduced by the laser treatment.

Moreover, in order to further quantify the effect of laser patterning on the corrosion rates, an ICP analysis of salts after the corrosion tests was performed (Fig. 15). ICP analysis was initially carried out on the samples shown in Fig. 7. However, no considerable difference was observed between the reference sample and the LTS. This was attributed to excessive peeling in the non-patterned areas of the LTS coupled with a high variance of the technique (Fig. 7). To this end, ICP was carried out in fully-patterned samples (Fig. 14, right). No Cr is detected in the salt after contact with the LTS sample. On the contrary, the salt after the corrosion test with reference SS310 contains a non-negligible amount of Cr. This translates to high Cr dissolution during the corrosion test. The salt, in contact with LTS, contains more Fe and Mn, after the corrosion test, which is in agreement with the cross-section analysis, where it can be seen that $FeCO_3$ and $Fe_{0.25}Mn_{1.4}C_{0.6}$ constitute the outer part of the corrosion layer, which is exposed to the molten salt (Fig. 12).

2.3. Mechanism discussion

The data presented above suggest that laser surface treatment can potentially inhibit corrosion of SS310, particularly in longer timeframes.

The corrosion resistance of common alloy elements in molten salts is of the order of Cr < Fe < Ni. These elements react with the O^{-2} and form corresponding $LiCrO_2$ Li(Fe, Ni)$_5O_8$ and Li(*Fe*, *Ni*)O_2 oxides through known reactions. The latter two, however, are known not to offer substantial corrosion protection [29]. The cross-section analysis (Fig. 8a) proves this, as the Li(Fe,Ni)$_5O_8$ and Li(*Fe*,*Ni*)O_2 oxides do not feature protective properties, and the underlying $LiCrO_2$ oxide tends to dissolve in the molten carbonate salt. This is evidenced by the fact that the chromium oxide layer is present on the surface of the metal in some spots, whereas it has been completely dissolved in others. This is further established from the ICP analysis (Fig. 14), which indicates Cr in the salt only in the case of non-treated samples.

Dissolution of chromium oxide in the molten salt is known to increase its basicity, which can then further amplify corrosion. The basicity of the ternary carbonates is of the following order Li_2CO_3 > $Na2CO_3$ > $K2CO_3$ [17]. This has also been confirmed by a recent ICP analysis of ternary carbonates in contact with SS310 [40]. Indeed the low molecular weight and smaller size of the Li + ion enable its diffusion and formation of oxide layers that are visible in the cross-sectional analysis (SEM analysis). In nitrate salts, Sun et al. argued that Cr correlated to higher content of NO_2- in SS samples in contact with SS304. Cr was found to be oxidized by NO_3- and thus promote decomposition of molten salts [41].

Numerous studies have reported the wettability transition of laser-induced femto-and nanostructured metal oxide surfaces exhibiting non-wetting behaviour over time in ambient air without the use of coating agents. Several mechanisms have been proposed to explain this. Kietzig et al. suggested that the catalyzed decomposition of carbon dioxide into carbon on laser-produced active magnetite, which was responsible for the observed wettability transition of laser-ablated metal alloys [42]. This was also noted by Žemaitis et al., who observed CO_2 decomposition following a reaction with a non-stoichiometric oxygen-deficient active magnetite $Fe_3O_{4-\delta}$, which was created during the laser irradiation process [43]. Long et al., on the other hand, indicated that CO_2, O_2 and N_2 atmospheres had little influence on the transition to a non-wetting state and, on the contrary, were restraining. They further proposed that organic compounds in the air play a vital role in this transition process and verified an increase in C-C(H) bond content after the laser treatment [44,45]. Yang et al. further confirmed this by demonstrating a 70.52 % increase of C-C(H) functional groups on a nanosecond laser textured Inconel surface after exposure to air for 30 days. In conjunction with the surface architecture, these chemisorbed organic compounds were found to be the mechanisms behind the wettability increase [46].

Indeed, FTIR analysis of the surface before and after being subjected to nanosecond laser processing reveals an increase in the intensity at wavenumbers corresponding to hydrophobic organic groups that match signals of long-chain hydrocarbons (Fig. 15). The data indicated that these groups are present only on the surface of the laser-treated SS310, not the untreated pristine surface or the one subjected to corrosion testing. Research has shown an increased number of airborne hydrocarbons present in chemical laboratories, particularly alkanes [47].

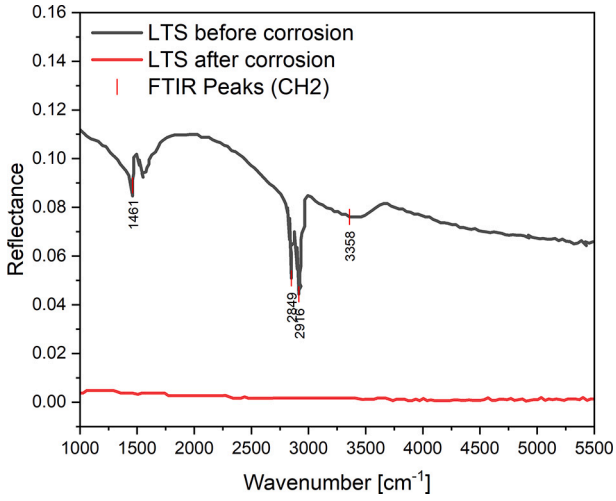

Fig. 15. FTIR analysis of the LTS SS310 before and after 600 h of corrosion test at 600 °C.

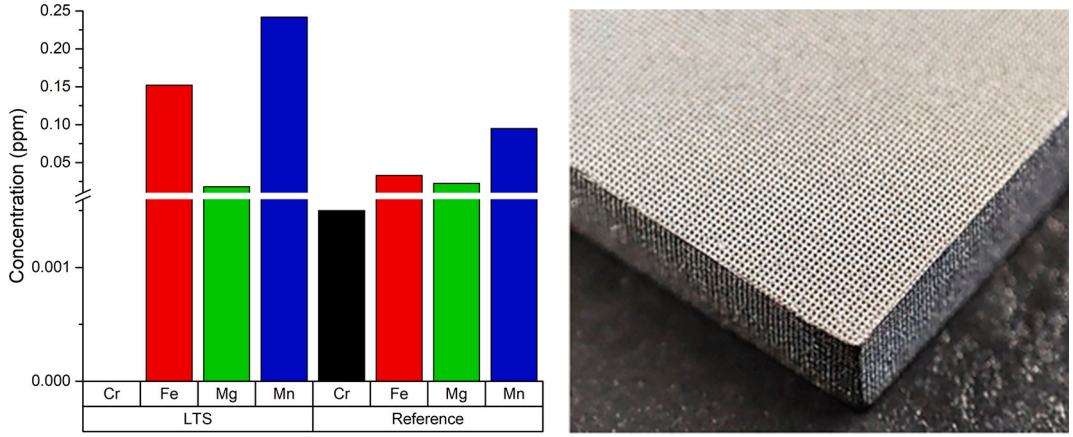

Fig. 14. Left: ICP analysis for molten salts after the corrosion tests with reference SS310 and LTS SS310; Right: Fully patterned LTS.

Adsorption of hydrocarbons of various lengths on metallic surfaces has already been reported [48]. Depending on their length, these can decompose into carbon at different annealing temperatures [49,50]. This carbon reacts with iron in the stainless steel and is transformed into iron carbides and carbonates during the corrosion test. Evidence of this is the formation of a $Fe_{0.25}$ $Mn_{1.4}C_{0.6}$ layer in the laser-treated sample, apart from the aforementioned oxide – Fig. 11. This layer was formed according to known reaction pathways identified in spray graphitization [51]. This reaction has been shown to release CO_2, which helps stabilize salt corrosion and further promotes the formation of carbides. These carbides and carbonates overall work favourably towards corrosion stabilization. Indeed, the oxide layers in the case of the laser-textured sample are much denser, reflected in the inward diffusion of Li+, which is considerably inhibited compared to the untextured surface. On the plain surface, the inhomogeneity is evidenced by the formation of mixed corrosion products further from the surface. This multi-structured corrosion scale is more prevalent to cracking, due to the difference in the thermal expansion of the various corrosion products [18]. This cracking then results in easier peel-off. Such cracking is observed in the case where the outward chromium oxide layer has peeled off and the gap between the outward iron oxide layer and the chromium layer beneath it is evident. This contrast with respect to peeling can be visualized when comparing Figs. 1 and 7(a), where peeling on the pristine unprocessed edges of the laser treated sample is evident. In contrast, peeling of the textured area is minimal.

3. Conclusion

In this work, nanosecond laser treatment was investigated, for the first time, as an approach solution to corrosion inhibition in molten carbonate salts. Plain and textured SS310 substrates were immersed statically for 600 h in Li_2CO_3-Na_2CO_3-K_2CO_3 at 600 °C under an air atmosphere. After analysing the samples, the following major insights were drawn:

1. Laser treatment leads to the adhesion of organic groups in the form of hydrocarbons on the SS310 surface. During the corrosion test, they decompose and contribute to forming carbonates and carbides.
2. Under the investigated conditions, no reduction in the corrosion rate is observed when comparing the untreated with the laser-treated samples; 26.9 ± 4.8 μm and 26.6 ± 2.47 μm for LTS and reference SS310 samples, respectively (roughly 390 μm/annually).
3. However, laser processing reduces peel-off and results in an overall improved denser corrosion product layer.
4. This layer inhibits the inward diffusion of lithium, thus preventing the dissolution of chromium in the molten salt, which in turn stabilizes the chromium oxide layer improving corrosion performance. ICP analysis further confirms this. Such improvement is anticipated to be highly relevant under dynamic conditions, where displacement of salt with respect to construction material greatly enhances peel-off and chromium dissolution.

Future work will be focused on dynamic conditions and longer timeframes where the stability of the chromium oxide layer and the reduced peel-off can further demonstrate the benefit of this processing protocol in corrosion inhibition for high-temperature molten salt applications.

Funding

All of the sources of funding for the work described in this publication are acknowledged in the manuscript.

Intellectual property

We confirm that we have given due consideration to the protection of intellectual property associated with this work and that there are no impediments to publication, including the timing of publication, with respect to intellectual property. In so doing we confirm that we have followed the regulations of our institutions concerning intellectual property.

CRediT authorship contribution statement

All listed authors meet the “Journal of Energy Storage” criteria. We attest that all authors contributed significantly to the creation of this manuscript, each having fulfilled criteria as established by the “Journal of Energy Storage”. We confirm that the manuscript has been read and approved by all named authors. We confirm that the manuscript has been read and approved by all named authors.

Declaration of competing interest

We wish to confirm that there are no known conflicts of interest associated with this publication and there has been no significant financial support for this work that could have influenced its outcome.

Data availability

Data will be made available on request.

References

[1] K. Ravi Kumar, N.V.V. Krishna Chaitanya, N. Sendhil Kumar, Solar thermal energy technologies and its applications for process heating and power generation – a review, J. Clean. Prod. (2020), 125296, https://doi.org/10.1016/j.jclepro.2020.125296.
[2] B. Koçak, A.I. Fernandez, H. Paksoy, Review on sensible thermal energy storage for industrial solar applications and sustainability aspects, Sol. Energy 209 (2020) 135–169, https://doi.org/10.1016/j.solener.2020.08.081.
[3] A. Bielecki, S. Ernst, W. Skrodzka, I. Wojnicki, Concentrated solar power plants with molten salt storage: economic aspects and perspectives in the European union, Int. J. Photoenergy. 2019 (2019), https://doi.org/10.1155/2019/8796814.
[4] Renewables 2020 Global Status Report, Renewables Global Status Report, 2020.
[5] M. Mehos, C. Turchi, J. Vidal, M. Wagner, Z. Ma, C. Ho, W. Kolb, C. Andraka, A. Kruizenga, Concentrating solar power Gen3 demonstration roadmap, 2017, https://doi.org/10.2172/1338899.
[6] Y.L. He, Y. Qiu, K. Wang, F. Yuan, W.Q. Wang, M.J. Li, J.Q. Guo, Perspective of concentrating solar power, Energy 198 (2020), https://doi.org/10.1016/j.energy.2020.117373.
[7] C. Villada, A. Toro, F. Bolívar, Corrosion performance of austenitic stainless steel SS304 in molten nitrate salts and Raman microscopy for stability analysis in thermal energy storage applications, J. Energy Storage 44 (2021), 103465, https://doi.org/10.1016/J.EST.2021.103465.
[8] A. Caraballo, S. Galán-Casado, Á. Caballero, S. Serena, Molten salts for sensible thermal energy storage: a review and an energy performance analysis, Energies 14 (2021), https://doi.org/10.3390/en14041197.
[9] A.G. Fernández, L.F. Cabeza, Corrosion evaluation of eutectic chloride molten salt for new generation of CSP plants. Part 2: materials screening performance, J. Energy Storage 29 (2020), 101381, https://doi.org/10.1016/J.EST.2020.101381.
[10] A.G. Fernández, L.F. Cabeza, Corrosion evaluation of eutectic chloride molten salt for new generation of CSP plants. Part 1: thermal treatment assessment, J. Energy Storage 27 (2020), 101125, https://doi.org/10.1016/J.EST.2019.101125.
[11] N.S. Patel, V. Pavlík, M. Boča, High-temperature corrosion behavior of superalloys in molten salts–a review, Crit. Rev. Solid State Mater. Sci. 42 (2017) 83–97, https://doi.org/10.1080/10408436.2016.1243090.
[12] G. Mohan, M.B. Venkataraman, J. Coventry, Sensible energy storage options for concentrating solar power plants operating above 600 °C, Renew. Sust. Energ. Rev. 107 (2019), https://doi.org/10.1016/j.rser.2019.01.062.
[13] R. Coyle, T.M. Thomas, P. Schissel, Corrosion of Selected Alloys in Eutectic Lithium-Sodium-Potassium Carbonate at 900 oC, 1986. Golden, Colorado.
[14] K. Takeuchi, A. Nishijima, K. Ui, N. Koura, C.-K. Loong, Corrosion behavior of Fe-Cr alloys in Li2CO3-K2CO3 molten carbonate, J. Electrochem. Soc. 152 (2005) B364, https://doi.org/10.1149/1.1955168.
[15] S. Ahn, K. Oh, M. Kim, J. Youn, K. Jo, K. Kim, H. Kwon, Electrochemical analysis on the growth of oxide formed on stainless steels in molten carbonate at 650 °C, Int. J. Hydrog. Energy (2014), https://doi.org/10.1016/j.ijhydene.2014.03.207.
[16] M.T. de Miguel, V. Encinas-Sánchez, M.I. Lasanta, G. García-Martín, F.J. Pérez, Corrosion resistance of HR3C to a carbonate molten salt for energy storage applications in CSP plants, Sol. Energy Mater. Sol. Cells 157 (2016) 966–972, https://doi.org/10.1016/j.solmat.2016.08.014.
[17] V. Encinas-Sánchez, M.T. de Miguel, G. García-Martín, M.I. Lasanta, F.J. Pérez, Corrosion resistance of Cr/Ni alloy to a molten carbonate salt at various

temperatures for the next generation high-temperature CSP plants, Sol. Energy 171 (2018), https://doi.org/10.1016/j.solener.2018.06.091.
[18] J. Luo, C.K. Deng, N. ul H. Tariq, N. Li, R.F. Han, H.H. Liu, J.Q. Wang, X.Y. Cui, T. Y. Xiong, Corrosion behavior of SS316L in ternary Li2CO3–Na2CO3–K2CO3 eutectic mixture salt for concentrated solar power plants, Sol. Energy Mater. Sol. Cells 217 (2020), https://doi.org/10.1016/j.solmat.2020.110679.
[19] S.P. Sah, E. Tada, A. Nishikata, Corrosion behaviour of austenitic stainless steels in carbonate melt at 923 K under controlled CO2-O2 environment, Corros. Sci. 133 (2018), https://doi.org/10.1016/j.corsci.2018.01.031.
[20] J. Gallardo-González, M. Martínez, C. Barreneche, A.I. Fernández, M. Liu, N.H. S. Tay, F. Bruno, M. Segarra, Corrosion of AISI316 as containment material for latent heat thermal energy storage systems based on carbonates, Sol. Energy Mater. Sol. Cells 186 (2018), https://doi.org/10.1016/j.solmat.2018.06.003.
[21] M. Sarvghad, T. Chenu, G. Will, Comparative interaction of cold-worked versus annealed Inconel 601 with molten carbonate salt at 450 °C, Corros. Sci. 116 (2017), https://doi.org/10.1016/j.corsci.2017.01.004.
[22] M. Sarvghad, O. Muránsky, T.A. Steinberg, J. Hester, M.R. Hill, G. Will, On the effect of cold-rolling on the corrosion of SS316L alloy in a molten carbonate salt, Sol. Energy Mater. Sol. Cells 202 (2019), https://doi.org/10.1016/j.solmat.2019.110136.
[23] M. Sarvghad, S. Bell, R. Raud, T.A. Steinberg, G. Will, Stress assisted oxidative failure of Inconel 601 for thermal energy storage, Sol. Energy Mater. Sol. Cells 159 (2017), https://doi.org/10.1016/j.solmat.2016.10.008.
[24] U. Nithiyanantham, Y. Grosu, A. Anagnostopoulos, E. Carbó-Argibay, O. Bondarchuk, L. González-Fernández, A. Zaki, J.M. Igartua, M.E. Navarro, Y. Ding, A. Faik, Nanoparticles as a high-temperature anticorrosion additive to molten nitrate salts for concentrated solar power, Sol. Energy Mater. Sol. Cells 203 (2019), https://doi.org/10.1016/j.solmat.2019.110171.
[25] J.C. Gomez-Vidal, Corrosion resistance of MCrAlX coatings in a molten chloride for thermal storage in concentrating solar power applications, npj Mater. Degrad. 1 (2017) 7, https://doi.org/10.1038/s41529-017-0012-3.
[26] A. Agüero, P. Audigié, S. Rodríguez, V. Encinas-Sánchez, M.T. de Miguel, F. J. Pérez, in: Protective coatings for high temperature molten salt heat storage systems in solar concentration power plants, 2018, p. 090001, https://doi.org/10.1063/1.5067095.
[27] S. Frangini, S. Loreti, The role of alkaline-earth additives on the molten carbonate corrosion of 316L stainless steel, Corros. Sci. 49 (2007) 3969–3987, https://doi.org/10.1016/j.corsci.2007.05.005.
[28] Y. Grosu, U. Nithiyanantham, A. Zaki, A. Faik, A simple method for the inhibition of the corrosion of carbon steel by molten nitrate salt for thermal storage in concentrating solar power applications, npj Mater. Degrad. 2 (2018) 34, https://doi.org/10.1038/s41529-018-0055-0.
[29] Y. Grosu, A. Anagnostopoulos, M.E. Navarro, Y. Ding, A. Faik, Inhibiting hot corrosion of molten Li2CO3-Na2CO3-K2CO3 salt through graphitization of construction materials for concentrated solar power, Sol. Energy Mater. Sol. Cells (2020), https://doi.org/10.1016/j.solmat.2020.110650.
[30] P. Kondaiah, R. Pitchumani, Fractal textured surfaces for high temperature corrosion mitigation in molten salts, Sol. Energy Mater. Sol. Cells 230 (2021), https://doi.org/10.1016/j.solmat.2021.111281.
[31] L.R. de Lara, R. Jagdheesh, J.L. Ocaña, Corrosion resistance of laser patterned ultrahydrophobic aluminium surface, Mater. Lett. 184 (2016), https://doi.org/10.1016/j.matlet.2016.08.022.
[32] S. Jana, M. Olszta, D. Edwards, M. Engelhard, A. Samanta, H. Ding, P. Murkute, O. B. Isgor, A. Rohatgi, Microstructural basis for improved corrosion resistance of laser surface processed AZ31 Mg alloy, Corros. Sci. 191 (2021), https://doi.org/10.1016/j.corsci.2021.109707.
[33] P. Pou-Álvarez, A. Riveiro, X.R. Nóvoa, M. Fernández-Arias, J. del Val, R. Comesaña, M. Boutinguiza, F. Lusquiños, J. Pou, Nanosecond, picosecond and femtosecond laser surface treatment of magnesium alloy: role of pulse length, Surf. Coat.Technol. 427 (2021), https://doi.org/10.1016/j.surfcoat.2021.127802.
[34] Z. Fan, X. Sun, X. Zhuo, X. Mei, J. Cui, W. Duan, W. Wang, X. Zhang, L. Yang, Femtosecond laser polishing yttria-stabilized zirconia coatings for improving molten salts corrosion resistance, Corros. Sci. 184 (2021), https://doi.org/10.1016/j.corsci.2021.109367.
[35] Z. Xia, Y. Xiao, Z. Yang, L. Li, S. Wang, X. Liu, Y. Tian, Droplet impact on the superhydrophobic surface with micro-pillar arrays fabricated by hybrid laser ablation and silanization process, Materials 12 (2019), https://doi.org/10.3390/ma12050765 (Basel).
[36] D. Huerta-Murillo, A. García-Girón, J.M. Romano, J.T. Cardoso, F. Cordovilla, M. Walker, S.S. Dimov, J.L. Ocaña, Wettability modification of laser-fabricated hierarchical surface structures in Ti-6Al-4V titanium alloy, Appl. Surf. Sci. 463 (2019), https://doi.org/10.1016/j.apsusc.2018.09.012.
[37] J.T. Cardoso, A. Garcia-Girón, J.M. Romano, D. Huerta-Murillo, R. Jagdheesh, M. Walker, S.S. Dimov, J.L. Ocaña, Influence of ambient conditions on the evolution of wettability properties of an IR-, ns-laser textured aluminium alloy, RSC Adv. 7 (2017), https://doi.org/10.1039/c7ra07421b.
[38] X.C. Wang, B. Wang, H. Xie, V. Kumar, R. Verma, V.S. Sharma, R.Samuel Sanjay Raja, P. Selvakumar, P.Dinesh Babu, B.Jacob Rubasingh, K. Suresh, Influence of laser parameters on superhydrophobicity- a review, al -, Eng. Res. Express 3 (2021), 022001, https://doi.org/10.1088/2631-8695/ABF35F.
[39] M.V. Rukosuyev, J. Lee, S.J. Cho, G. Lim, M.B.G. Jun, One-step fabrication of superhydrophobic hierarchical structures by femtosecond laser ablation, Appl. Surf. Sci. 313 (2014) 411–417, https://doi.org/10.1016/J.APSUSC.2014.05.224.
[40] L. González-Fernández, M. Intxaurtieta-Carcedo, O. Bondarchuk, Y. Grosu, Effect of dynamic conditions on high-temperature corrosion of ternary carbonate salt for thermal energy storage applications, Sol. Energy Mater. Sol. Cells 240 (2022), 111666, https://doi.org/10.1016/J.SOLMAT.2022.111666.
[41] Z. Sun, Y. Luo, P. Song, X. Gao, Acceleration of thermal decomposition of molten nitrates by Cr in steel and promotion of this effect by halogens, AIChE J. (2022), https://doi.org/10.1002/aic.17905.
[42] A.-M. Kietzig, S.G. Hatzikiriakos, P. Englezos, Patterned superhydrophobic metallic surfaces, 2009, https://doi.org/10.1021/la8037582.
[43] A. Žemaitis, A. Mimidis, A. Papadopoulos, P. Gečys, G. Račiukaitis, E. Stratakis, M. Gedvilas, Controlling the wettability of stainless steel from highly-hydrophilic to super-hydrophobic by femtosecond laser-induced ripples and nanospikes, RSC Adv. 10 (2020) 37956–37961, https://doi.org/10.1039/D0RA05665K.
[44] J. Long, M. Zhong, H. Zhang, P. Fan, Superhydrophilicity to superhydrophobicity transition of picosecond laser microstructured aluminum in ambient air, J. Colloid Interface Sci. 441 (2015) 1–9, https://doi.org/10.1016/J.JCIS.2014.11.015.
[45] J. Long, P. Fan, D. Gong, D. Jiang, H. Zhang, L. Li, M. Zhong, Superhydrophobic surfaces fabricated by femtosecond laser with tunable water adhesion: from lotus leaf to rose petal, 2015, https://doi.org/10.1021/acsami.5b01870.
[46] Z. Yang, Y. Tian, Y. Zhao, C. Yang, Study on the fabrication of super-hydrophobic surface on Inconel alloy via nanosecond laser ablation, Materials 12 (2019), https://doi.org/10.3390/ma12020278 (Basel).
[47] C.J. Illing, C. Hallmann, K.E. Miller, R.E. Summons, H. Strauss, Airborne hydrocarbon contamination from laboratory atmospheres, Org. Geochem. 76 (2014), https://doi.org/10.1016/j.orggeochem.2014.07.006.
[48] S. Lehwald, H. Ibach, Decomposition of hydrocarbons on flat and stepped Ni(111) surfaces, Surf. Sci. 89 (1979) 425–445, https://doi.org/10.1016/0039-6028(79)90628-9.
[49] J. Wintterlin, M.L. Bocquet, Graphene on metal surfaces, Surf. Sci. 603 (2009) 1841–1852, https://doi.org/10.1016/J.SUSC.2008.08.037.
[50] S. Ahmed, A. Aitani, F. Rahman, A. Al-Dawood, F. Al-Muhaish, Decomposition of hydrocarbons to hydrogen and carbon, Appl. Catal. A Gen. 359 (2009) 1–24, https://doi.org/10.1016/J.APCATA.2009.02.038.
[51] Y. Zhang, D.M. Schleich, Preparation and characterization of iron manganese carbide by reaction of the oxides and carbon in nitrogen, J. Solid State Chem. 110 (1994) 270–273, https://doi.org/10.1006/JSSC.1994.1169.